Oxidation State Dependent Conjugation Controls Electrocatalytic Activity in a Two-Dimensional Di-Copper Metal–Organic Framework

Maria Dominic, A.; Wang, Z.; Kuc, A. B.; Petkov, P.; Khoa Ly, H.; Lam Huong Pham, T.; Kutzschbach, M.; Cao, Y.; Bachmann, J.; Feng, X.; Dong, R.; Weidinger, I. M.;

Originally published:

April 2023

Journal of Physical Chemistry C 127(2023), 7299-7307

DOI: https://doi.org/10.1021/acs.jpcc.2c08819

Correlating oxidation states and electrocatalytic activity in bifunctional two-dimensional conjugated di-copper metal-organic frameworks

Journal:	*Journal of the American Chemical Society*
Manuscript ID	ja-2022-05895w
Manuscript Type:	Article
Date Submitted by the Author:	03-Jun-2022
Complete List of Authors:	Dominic, Anna; Technische Universitat Dresden, Chemistry Wang, Zhiyong; TU Dresden, Kuc, Agnieszka; Helmholtz-Zentrum Dresden-Rossendorf, Petkove, Petko St. ; Sofia University St Kliment Ohridski Faculty of Chemistry and Pharmacy Ly, Khoa; Technische Universitat Dresden, Chemistry Cao, Yuanyuan; Friedrich-Alexander Universität Erlangen-Nürnberg (FAU), Chemistry and Pharmacy, Chemistry of Thin Film Materials. Interdisciplinary Center for Nanostructured Films (IZNF) Bachmann, Julien; Friedrich-Alexander-Universitat Erlangen-Nurnberg, Department of Chemistry and Pharmacy Pham, Thi Lam ; TU Berlin Institute of Ecology Kutzschbach, Martin ; TU Berlin Institute of Ecology Feng, Xinliang; Technische Universitat Dresden, Molecular Functional Materials Dong, Renhao; TU Dresden, Faculty of Chemistry and Food Chemistry Weidinger, Inez; Technische Universitat Dresden, Chemistry

Correlating oxidation states and electrocatalytic activity in bifunctional two-dimensional conjugated di-copper metal-organic frameworks

Anna Maria Dominic[1], Zhiyong Wang[1,6], Agnieszka Kuc[2], Petko Petkov[3], Khoa Hoang Ly[1], Thi Lam Huong Pham[4], Martin Kutzschbach[4], Yuanyuan Cao[5], Julien Bachmann[5], Xinliang Feng[1,6], Renhao Dong[1], Inez M. Weidinger*[1]

[1]Technische Universität Dresden, Faculty of Chemistry and Food Chemistry, 01062 Dresden, Germany

[2]Helmholtz-Zentrum Dresden-Rossendorf, Abteilung Ressourcenökologie, Forschungsstelle Leipzig, Leipzig, Germany

[3]University of Sofia, Faculty of Chemistry and Pharmacy, 1164 Sofia, Bulgaria

[4]Institute of Ecology, Berlin University of Technology, Berlin, Germany

[5]Friedrich-Alexander-Universität Erlangen-Nürnberg, Department of Chemistry and Pharmacy, Chemistry of thin films

[6]Max Planck Institute for Microstructure Physics, Weinberg 2, Halle (Saale), D-06120 Germany

ABSTRACT: Molecularly defined materials have a bright future in electrocatalysis, but an understanding of the molecular processes under operando conditions is urgently needed for rational optimization of these systems. For this purpose, copper-phthalocyanine-based two-dimensional conjugated metal-organic framework (CuPc-CuO_4 2D c-MOF) films with an edge-on layer orientation were transferred to graphite electrodes and analyzed via electrochemical resonance Raman spectroscopy. Comparison of CuPc-CuO_4 with the corresponding monomer, combined with Density Functional Theory (DFT) calculations allowed a detailed assignment of the vibrational bands. CuPc-CuO_4 films attached to graphite electrodes via a nickel-nitrilo triaacetic acid (Ni-NTA) linker exhibited excellent bifunctional catalytic activity towards oxygen reduction (ORR) and oxygen evolution reaction (OER). Potential dependent Raman spectroscopy yielded three different species in the respective potential window that could be assigned to an ORR active Cu^{I}/Cu^{I} state, an inactive Cu^{II}/Cu^{I} state, and a Cu^{II}/Cu^{II} state that could be activated for OER. From the spectroelectrochemical data, the redox potentials of the Cu in the CuPc moieties and the Cu-catecholate nodes could be determined to be E_{CuPc} = -0.04V and E_{CuO4} = 0.33 V vs. Ag|AgCl, respectively. Furthermore, DFT calculations of bandgaps and density of states (DOS) showed the smallest bandgap and highest π-conjugation for the Cu^{I}/Cu^{I} state and the largest bandgap and lower conjugation for the mixed Cu^{II}/Cu^{I} state, agreeing very well with the experimental activity of the species. Our results suggest that the coupling between metal oxidation changes and long-range electron transfer of the 2D c-MOF is a key parameter towards achieving high electrocatalytic activity.

Introduction

Electrochemical devices can be operated using renewable energy sources and thus have become the main alternative to devices that rely on fossil fuel combustion. Fuel cells, water electrolyzers and metal-air batteries require the electrocatalytic transformation of oxygen and in the best case both, the oxygen reduction reaction (ORR) and the oxygen evolution reaction (OER) can be performed by the same electrode material upon a change in applied bias. Precious metal catalysts based on Pt and IrO_2/RuO_2 are by far considered as the best candidates for ORR and OER respectively.[1,2] But their resource exhaustion and high price are the bottlenecks for extended commercial use. Several carbon-based[3,4] and non-precious transition-metal[5,6] containing molecular complexes, on the other hand, have been developed that are capable of catalyzing ORR and OER with decent turnover frequencies. However, these systems exhibit in general very inefficient intermolecular electron transfer, which results in overall low current densities. In an alternative approach, transition metals are incorporated in conductive nitrogen-doped carbon matrixes resulting in catalytically active metal-nitrogen ($M-N_x$) sites.[7,8] While this strategy has led to very efficient oxygen transforming catalysts, the amount and distribution of active sites are difficult to control. Therefore, molecular bottom-up approaches using molecular units as building blocks have great potential towards improving electrode design beyond the state of the art. Suitable molecular building blocks are metal phthalocyanines (MPcs), which offer a unique conjugated structure that can provide π electrons during catalysis.[9] There have been several reports of MPc-based materials that show bifunctional catalysis of oxygen involving reactions (ORR and OER).[10–13] Surprisingly, none of these pieces of work has included copper (CuPc) catalysts, albeit some work on bifunctional Cu-molecular complexes has been published in the literature.[14] However, since Cu is an earth-abundant element and the second least expensive first-row transition metal, it would be highly advantageous to develop CuPc based molecular ORR/OER catalysts.[15,16]

Metal-organic frameworks (MOFs) are porous hybrid materials consisting of coordination bonds between multidentate organic linkers and metal cations.[17] The high precision in material synthesis and extensive variability of building blocks allow them to be optimized for various

applications such as gas storage or electronics.[18] Among them, two-dimensional conjugated MOFs (2D c-MOFs) have shown excellent potential for electrocatalytic applications as they exhibit good ion diffusion ability and fully in-plane π-delocalisation,[19,20] thereby overcoming the usually low conductivity of MOFs. Upon variation of the central metals, a large number of 2D c-MOFs have been developed recently that were specifically optimized for hydrogen evolution reaction (HER), OER, ORR and carbon dioxide reduction reaction (CO_2RR).[21]

For rational design of MOF electrocatalysts, a fundamental understanding of their redox and catalytic reaction mechanism is mandatory. In-situ Raman spectroscopy is ideally suited to provide that information as it can be easily applied in an aqueous solution and under the influence of electric potential. Combining Raman spectroscopy with electrochemical data on the same system allows correlating electrocatalytic activity with structural changes of the material during catalysis and has been utilized to identify active sites and determine reaction mechanisms.[22–24]

Herein, we have attached an edge-on layer oriented CuPc-based 2D c-MOF film with Cu-catecholates (CuPc-CuO_4) [25] via a Ni-NTA linker to a smooth graphite electrode, which exhibited increased bifunctional catalytic activity towards ORR and OER. We were able to employ operando electrochemical resonance Raman spectroscopy to investigate the redox properties of the Cu species at the CuPc moieties and CuO_4 linkages during the catalytic processes. The experimental data was supported by theoretical Density Functional Theory (DFT) calculations of Cu^{I} and Cu^{II} oxidation states. Additionally, the bandgap energies and density of states (DOS) of the different states have been calculated to correlate the π-conjugation with the metal's oxidation states.

Results and Discussion

According to our previous report,[25] 2, 3, 9, 10, 16, 17, 23, 24 -octahydroxy phthalocyaninato Cu (CuPc-$(OH)_8$) monomer was employed as a ligand to construct the CuPc-CuO_4 2D c-MOF film on the water surface (Figure 1). The as-prepared film was then transferred onto substrates. The preferential edge-on orientation of the CuPc-CuO_4 film was determined by imaging and diffraction techniques.[25]

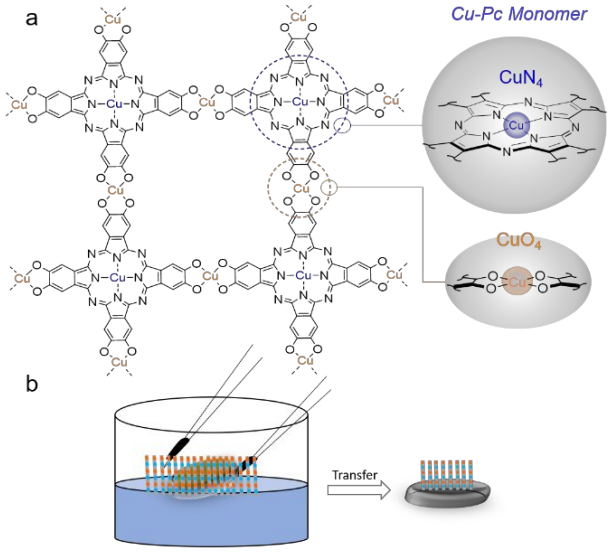

Figure 1. (a) Structure of CuPc-CuO_4, (b) Schematic illustration of the edge-on oriented CuPc-CuO_4 film on the water surface and transfer to solid electrodes.

By dipping a roughened silver (Ag) electrode through the air-water interface, the CuPc-CuO_4 film was attached to its surface. Since the UV-vis spectra of CuPc-CuO_4 showed absorbance maxima at 320 nm and 620 nm (Figure S1), laser excitation at 595 nm was used in resonance with the surface enhancement of the Ag electrode and the resonance Raman enhancement of CuPc-CuO_4, which allowed for a detailed analysis of the surface-attached CuPc-CuO_4 film via surface-enhanced resonance Raman spectroscopy (SERRS). For spectral comparison, the CuPc-$(OH)_8$ monomer self-assembled on the water surface was also attached to the Ag surface via the same procedure. The resulting SERR spectra at an electrode potential of 0.1 V vs. Ag|AgCl are shown in Figure 2.

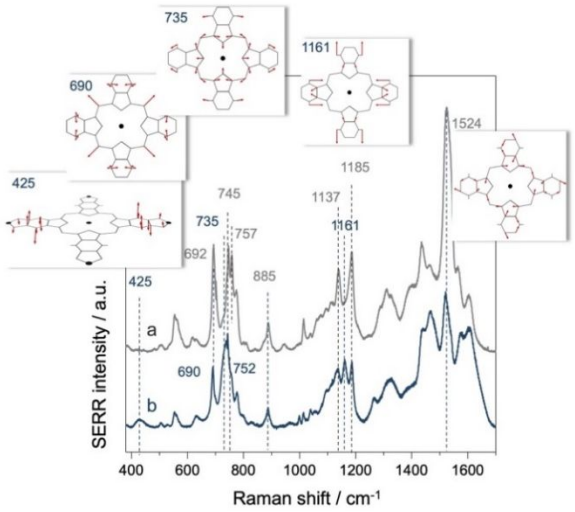

Figure 2. Surface-enhanced resonance Raman (SERR) spectra of the CuPc-$(OH)_8$ monomer (trace a) and the CuPc-CuO_4 MOF (trace b) at 0.1 V vs. Ag|AgCl (KCl 3M). Laser excitation: 595 nm. The insets illustrate the vibrations of selected vibrational modes as obtained from the DFT calculations

The spectral assignment was enabled by comparing the measured spectra with DFT calculations (Figure S2). Due to the enormous complexity of the spectral pattern, we will focus on the following selected bands that can be assigned confidently: Most importantly, a peak at 425 cm^{-1} rises in the CuPc-CuO_4 2D c-MOF that is absent in the calculated and measured spectra of the monomer. Two peaks at 402 and 464 cm^{-1} in the calculated CuPc-CuO_4 2D c-MOF spectrum can be assigned to this measured peak. Both represent out-of-plane vibrations that are only possible if a certain degree of polymerization has occurred. This makes them highly suitable marker bands to monitor the polymerization process. Between 600 and 900 cm^{-1}, a prominent band occurs at 745 cm^{-1} in the monomer that is shifted to 735 cm^{-1} in the MOF. In comparison with DFT calculations we assign this band to a totally symmetric vibration at 777 cm^{-1} which includes both the Pc-unit and the phenol ligands but with a main contribution from the Pc (see inset Figure 2). A neighboring band at 757 cm^{-1} can be seen in the monomer that is shifted to 752 cm^{-1} in the MOF, which is also assigned to vibration with a high contribution of the Pc. On the other hand, an isolated band at 887 cm^{-1} exists that does not shift upon polymerization. This band is also clearly present in the calculated spectra. Between 1000 and 1200 cm^{-1} two dominant bands at 1137 and 1185 cm^{-1} are seen in the monomer, whereas a third band at 1161 cm^{-1} is exhibited exclusively by the MOF. The shift to lower wavenumbers is confirmed in the calculations which predict a band-shift from 1173 to 1154 cm^{-1} in the monomer and MOF, respectively. We assign this band also to a combined Pc-phenol vibration, but in this case with a much higher contribution of the phenol rings and the CuO_4 linkages (see inset in Figure 2). Above 1200 cm^{-1}, a broad superposition of bands are seen that change in an unspecific manner upon polymerization. Also in this region, strong deviations between the calculated and measured spectra are observed. We, therefore, refrain from a more detailed assignment in this region. Note that the band at 1524 cm^{-1}, which is very dominant in the monomer, decreases significantly in intensity in the CuPc-CuO_4 2D c-MOF. The different modes are summarized in Table 1.

Table 1. Selected experimental and corresponding calculated Raman frequencies of a CuPc-CuO_4 2D c-MOF in cm^{-1}

Labeling	Monomer exp.	Monomer calc.	MOF exp.	MOF calc.
ν_a	n.v.	n.v.	425	464
ν_b	692	713	690	709
ν_c	745	772	735	777
ν_d	757	792	752	799
ν_e	887	887	887	887
ν_f	1137	n.v.	1135	1131
ν_g	1185	1173	1161	1154
ν_h	1524	1515	1524	1495

The labeling of the modes (ν_a- ν_h) is done to simplify their discussion in the text; nv: not visible

While Ag electrodes are best suited for enhancing the Raman signals of the adsorbed CuPc-CuO_4 2D c-MOF, their applicability in electrocatalysis is limited by their low oxidation potential and lesser abundance with respect to graphite electrodes as solid support materials. CuPc-CuO_4 2D c-MOFs were thus attached to graphite via dipping. The immobilization was in this case less efficient, but a low-quality Raman spectrum could still be detected (Figure 3, trace c). To improve the adhesion of the CuPc-CuO_4 to the graphite electrode the latter was functionalized with a nickel nitrilotriacetic acid (Ni-NTA) linker. Covalent attachment of the Ni-NTA was achieved by running reduction and oxidation cycles in Ni (II) nitrate aqueous solution containing N_α, N_α-bis-(carboxymethyl)-L-lysin hydrate following published procedures.[26] The modification of the graphite electrodes considerably enhanced the adhesion as demonstrated by the significantly increased Raman intensity of the CuPc-CuO_4 2D c-MOF (Figure 3, trace d). Note that the Ni-NTA alone did not yield any Raman signals. Scanning Electron Microscopy (SEM) images (Figure S3) showed an increased roughness of the Ni-NTA modified carbon surface after 2D c-MOF incubation pointing to a better attachment in this case. This was confirmed by Inductively Coupled Plasma -Mass Spectrometry (ICP-MS) measurements which yielded a Cu content of $0.6 \cdot 10^{-8}$ moles with and $0.06 \cdot 10^{-8}$ moles without prior Ni-NTA functionalization (for details see SI section 5). In the former case, an additional Ni content of $0.13 \cdot 10^{-8}$ M was measured.

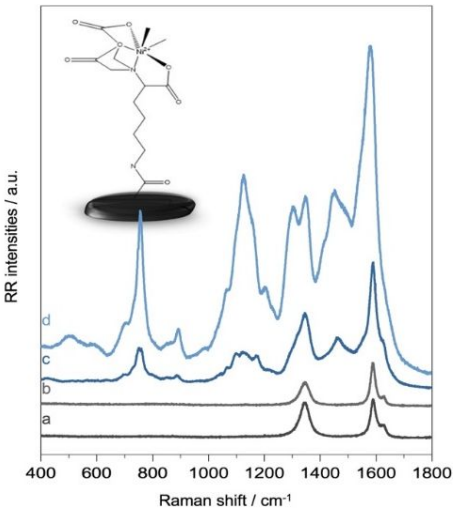

Figure 3. Raman spectra of (a) a bare graphite electrode, (b) a Ni-NTA functionalized graphite electrode, (c) CuPc-CuO_4 MOF on a bare graphite electrode and (d) CuPc-CuO_4 MOF on a Ni-NTA functionalized graphite electrode.

Figure 4a shows the in-situ Raman spectra of CuPc-CuO_4 on Ni-NTA modified graphite electrodes in 0.01 M H_2SO_4 under an inert atmosphere at different potentials (from 0.8 to -0.4 V *vs.* Ag|AgCl) in the frequency range from 400 to 1400 cm^{-1}. The high stability of the CuPc-CuO_4 2D c-MOF is proven by the identical spectra at 0.8 V before and after reduction (Figure S4). The spectrum resembles the one on Ag but with slightly shifted bands and lesser intensity. The peak at 425 cm^{-1} is barely visible but the peaks in the regions from 600 to 800 cm^{-1} and from 1100 to 1200 cm^{-1} are sufficiently intense to be analyzed. In the potential-dependent spectra, three species can be identified (Figure 4a). The same is true for the high-frequency range above 1400 cm^{-1} (Figure S5). Species III dominates at potentials above 0.4 V, in between 0.4 and -0.1 V, species II is present whereas species I becomes dominant below -0.1 V. The rise and fall of these species can be most clearly seen in the band shifts in the region between 690 and 750 cm^{-1}, the relative intensities of which are plotted exemplarily in Figure 4b. The data could be fitted using the Nernst equation yielding two redox potentials of $E_1 = 0.33 \pm 0.03$ V and $E_2 = -0.04 \pm 0.01$ V, respectively.

For both the bare and Ni-NTA functionalized CuPc-CuO_4 2D c-MOF-graphite systems, electrocatalytic activity in O_2 saturated water was tested using linear sweep voltammetry (LSV, Figure 4c). The CuPc-CuO_4 showed a bifunctional behavior with ORR activity below an onset potential of -0.1 V and OER activity above an onset potential of 0.55 V vs. Ag|AgCl. Furthermore, NTA grafting enhanced the electrocatalytic performance by 150% for the ORR and even 250% for the OER. For the CuPc-CuO_4 Ni-NTA system, an OER current density of 1 mA/cm^2 was reached at 0.8 V vs. Ag|AgCl (corresponding to an overpotential of η= 500 mV). Using the number of Cu atoms previously determined by ICP-MS we calculated the turnover frequency (TOF) at this potential to be 0.43 s^{-1} (for details see SI section 6).

In the following, we aim to assign the observed species I-III to their respective Cu/Cu oxidation states (in this notation the first Cu stands for the Pc-coordinated Cu ion and the second one for CuO_4 linkages). The CuPc under OCP conditions was determined recently to be present in its Cu^{II} oxidation state.[27] Redox titrations of selected bands of the CuPc-$(OH)_8$ monomer on rough Ag (Figure S6) showed a redox potential of the $Cu^{II} \rightarrow Cu^{I}$ transition to be at ca. -0.05 V vs. Ag|AgCl, which is close to our low potential redox transition at E_2=-0.04 V. We, therefore, assign species II to a Cu^{II}/Cu^{x} redox state, whereas species I refers to a Cu^{I}/Cu^{x} oxidation state.

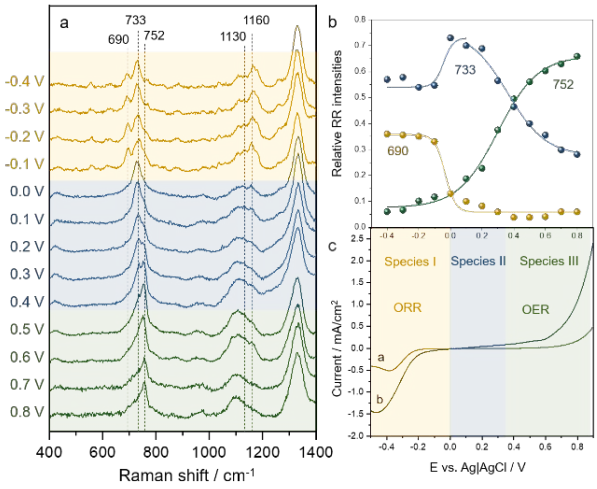

Figure 4. (a) Potential dependent Raman spectra of CuPc-CuO_4 on Ni-NTA modified graphite. Potentials are measured vs. Ag|AgCl reference electrode. (b) Analysis of peaks from 690 to 752 cm^{-1}. (c) LSV curves of CuPc-CuO_4 in O_2 saturated atmosphere in 0.1M KOH on graphite electrodes without (trace a) and with (trace b) Ni-NTA functionalization.

For further assignment of both Cu oxidation states, Raman spectra were computed for Cu^{I}/Cu^{I}, Cu^{II}/Cu^{I} and Cu^{II}/Cu^{II} (See Table 2 and Figure S7, S8). For the $Cu^{II}/Cu^{I} \rightarrow Cu^{I}/Cu^{I}$ transition no significant change is observed for the ν_c marker band (789/791 cm^{-1}). We assign this band to the experimentally detected band at 733 cm^{-1} (ν_c). However, exclusively for the Cu^{I}/Cu^{I} state, the vibration at 690 cm^{-1} (ν_b) occurs. Interestingly, theory predicts that this band should be present also for the other oxidations states with only minor shifts in frequency. However, in contrast to ν_c, the ν_b mode is highly polarization-dependent (Figure S9) and almost no contribution is expected for perpendicular polarization. We thus propose that the transformation into the Cu^{I}/Cu^{I} state goes hand in hand with a reversible re-orientation or scrambling of the preferential CuPc-CuO_4 2D c-MOF orientation. This interpretation is further supported by the observation of this band in other experimental setups, e.g., when adsorbed on rough Ag (see Figure 2) or in the presence of bound oxygen as shown in previous work. [27] For the $Cu^{II}/Cu^{I} \rightarrow Cu^{II}/Cu^{II}$ transition, calculations predict a redshift of the ν_c to 778 cm^{-1}, which is not seen a priori in the experimental data. However, the presence of the 733 cm^{-1} band even at very positive potential might account for this band (for simplicity, this peak area was fitted with three bands only). However, in the calculated spectra, the ν_d mode at 799 cm^{-1} is exclusively visible in the Cu^{II}/Cu^{II} state. Thus, we assign the band observed experimentally at 752 cm^{-1} to this mode.

The frequency region from 1100 to 1200 cm^{-1} shows distinct oxidation-dependent changes but due to the broad overlap, spectral analysis is very difficult and will be restricted to the previously assigned ν_f and ν_g modes (see Table 2). For the III $\rightarrow$ II transition only small changes are observed, whereas for the II $\rightarrow$ I transition more clearly defined peaks become visible but without any overall red- or blue-shift. Theory

predicts no significant changes for the Cu^{II}/Cu^{II} → Cu^{II}/Cu^{I} transition, which supports our hypothesis that this is equivalent to the III → II transition. However, for the Cu^{I}/Cu^{I} state, a clear redshift is expected for the ν_g mode, which at first sight does not correlate with the experimental spectra. However, theory predicts a concomitant blueshift for the ν_f mode. Both effects combined would result in an overall non-visible peak shift in that spectral region as observed in the measured EC-Raman spectra. The assignment of oxidation-dependent Raman bands is summarized in Table 2.

Table 2. Selected Raman vibrations in cm^{-1} and bandgap energies in eV for the different Cu oxidation states.

	Raman vibrations in cm^{-1}					
	Cu^{II}/Cu^{II}		Cu^{II}/Cu^{I}		Cu^{I}/Cu^{I}	
	exp.	calc.	exp.	calc.	exp.	calc.
ν_b	n.v.	709	n.v.	706	690	702
ν_c	733	778	733	789	733	791
ν_d	752	799	n.d.		n.d.	
ν_f	1129	1131	1126	1136	1157	1142
ν_g	1160	1154	1154	1155	1133	1120
	Bandgap in eV					
		0.92		1.25		0.51

Bandgap energies obtained at HSE06 level of theory; n.v: not visible ; n.d: not determined.

Based on the considerations discussed above we assign species III to the Cu^{II}/Cu^{II} state, species II to the Cu^{II}/Cu^{I} state and species I to the Cu^{I}/Cu^{I} state with the respective redox potentials of $E_{CuI \rightarrow CuII}$ = -0.04 V for the Cu in the Pc and $E_{CuI \rightarrow CuII}$ = 0.33V for Cu in the oxygen linkages. ORR usually starts from the Cu^{I} oxidation state. [28] In the present case, both Cu ions have to be in this state for efficient catalysis. An explanation for this can be derived by considering the bandgaps calculated for the 2D c-MOF in its different oxidation states (see Table 2 and Figure S10). Interestingly, the mixed-state (Cu^{II}/Cu^{I}) has the highest bandgap of 1.25 eV, whereas the Cu^{I}/Cu^{I} state exhibits a significantly reduced bandgap of 0.51 eV. Additional calculations of DOS (Figure 5 and Figure S11) projected on atom types reveal a contribution of Cu (from Pc units), C and N atoms in the frontier orbitals in the Cu^{I}/Cu^{I} state, but almost only of C atoms in the Cu^{II}/Cu^{I} state. Cu states in Cu^{II}/Cu^{I} are situated at least 0.5 eV below the Fermi energy level and 2.5 eV above it. These calculations suggest that fast electron transport between the active Cu sites is only possible in the Cu^{I}/Cu^{I} state and not in the Cu^{II}/Cu^{I} state. In this scenario, the CuPc might not function as a catalytic site for ORR, but it is needed to be in its Cu^{I} state to work as an electron transport unit. The transition to the Cu^{II}/Cu^{II} state is also accompanied by a lowering of the bandgap to 0.92 eV, which might be beneficial for fast electron removal from the active sites in OER.

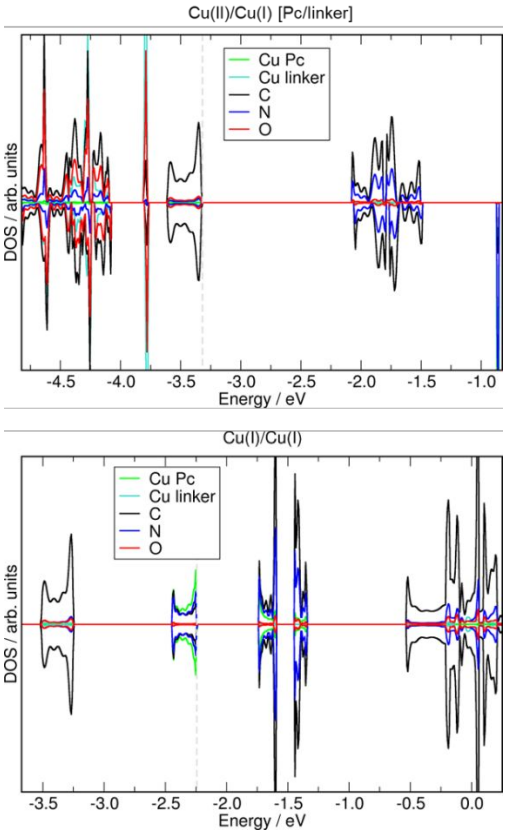

Figure 5. Density of states projected on atom types for the Cu^{II}/Cu^{I} (top) and Cu^{I}/Cu^{I} states (bottom). The dashed lines represent the Fermi level, set at the top of valence band.

Bifunctional electrocatalytic activity has been observed in the past for CoPc and FePc systems.[11] Also, OER activity involving the Cu^{III} state has been proposed for molecular Cu-containing catalysts.[29] CuPc compounds have not been presented as catalysts for OER so far. [30] Therefore, additional LSV measurements using CuPc-$(OH)_8$ monomers attached via Ni-NTA to the graphite electrode were performed that showed OER activity above an onset potential of 0.75 V vs. Ag|AgCl (Figure S12). Since we observe OER activity in the 2D c-MOF already at an onset potential of 0.55 V vs. Ag|AgCl, we conclude that OER starts with a Cu^{II}-Pc state present in this sample. Whether OER requires the formation of an Cu^{III} state in the oxygen linkages cannot be concluded from the data. Most likely, the Cu^{III}-O_4 state is transiently formed, but not visible in the steady state Raman spectra. The proposed reaction mechanism is summarized in Figure 6.

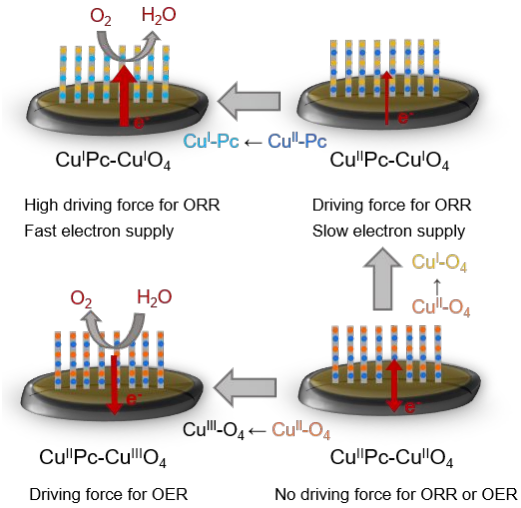

Figure 6. Proposed reaction mechanism based on the spectroelectrochemical data and calculations.

In conclusion, we have for the first time attached CuPc-CuO_4 2D c-MOFs to a Ni-NTA functionalized graphite electrode, which exhibited bifunctional electrocatalytic activity for oxygen reduction and evolution. The unique attachment via Ni-NTA linkers enabled us to measure Raman spectra of the CuPc-CuO_4 2D c-MOF on graphite as a function of applied potential. Comparison with calculated spectra allowed to determine the redox potentials of the Cu^{II} →Cu^{I} transition in the CuPc and the CuO_4 linkages to be E_{CuPc}= -0.04V and E_{CuO4}= 0.33 V respectively. We demonstrated that ORR requires a Cu^{I} state in both units. Calculations of the respective bandgaps of the material prepared in the various possible oxidation states yielded the highest value for the mixed-valent state and the lowest for the Cu^{I}/Cu^{I} state. This demonstrates that not only the oxidation state of the Cu units plays a crucial role in electrocatalysis but also the oxidation state-dependent π-conjugation of the whole CuPc-CuO_4 2D c-MOF. Furthermore, the data suggest a change in orientation or scrambling of the CuPc-CuO_4 2D c-MOF in the catalytically active Cu^{I}/Cu^{I} state. Whether this effect is beneficial for catalysis e.g., by promoting oxygen diffusion into the layers must be further examined in the future. Our results demonstrate the applicability of CuPc-CuO_4 2D c-MOFs as bifunctional electrocatalysts with potential use in metal-oxygen batteries and also give fundamental insight into the interplay between redox changes and MOF conjugation that can be used to further advance bimetallic MOFs in electrocatalysis.

Materials and Methods

CuPc-CuO_4 MOF Synthesis: 200 µL of freshly prepared solution of CuPc-$(OH)_8$ in chloroform/DMF (2:1 in volume) (1 mg ml^{-1}) was spread onto the water surface in a beaker under ambient conditions. A green film was formed after 30 mins on the water surface due to the self-assembly of CuPc-$(OH)_8$. Coordination polymerization was achieved by the addition of an aqueous solution of copper(II) acetate (5 ml, 1mg ml^{-1}) and sodium acetate (2 ml, 1 mg ml^{-1}) into the water subphase. After 18h, CuPc-CuO_4 2D c-MOF was obtained as translucent black thin films on the water surface which can be easily transferred to the electrodes.

Ni-NTA Modification of electrodes: A graphite disk electrode (1.2 cm in diameter) was first polished with alumina slurries (0.5 and 0.06 mm) and cleaned by sonication in Milli-Q water. After being cleaned with Milli-Q water, the electrode was immersed in 0.5 M sulfuric acid and scanned between 1 V and 1 V for 400 cycles at 200 mV s^{-1}. NTA–Ni^{2+} and NTA-Cu^{2+} then modified on the electrode surface by the cycling of GC electrode in 2 mM NTA–Ni^{2+} and NTA-Cu^{2+} solution between 500 mV and 1500 mV for about 200 scans at 200 mV s^{-1}. Following this, the interfacially synthesized CuPcCu MOFs are transferred to the modified electrode by dipping. The disc electrode, as the working electrode, was placed in a custom-made electrochemical cell, a platinum wire and an Ag/AgCl electrode were used as counter and reference electrodes respectively. Electrochemical experiments were conducted using an Ivium Vertex One EIS potentiostat with Ivium electrochemical software. Experiments were performed in 0.1 M KOH solution. During LSV measurements for OER and ORR, the sealed electrochemical cell was under continuous O_2 gas supply.

Resonance Raman spectroscopy was conducted using a confocal Raman microscope (S&I Monovista CRS+) with laser excitation by a Cobolt Mambo 594 nm diode laser. The laser was aligned and then focused on the sample using an Olympus 20× objective at a laser power of ≈1 mW. The sample stage was constantly moved during the measurement to avoid degradation. Spectra were calibrated with respect to the Raman spectrum of toluene. During the measurements, the cell was completely sealed, and a continuous flow of Ar gas was ensured.

All systems were fully optimized using the Vienna ab-initio Simulation Package (VASP).[31] The electronic wavefunctions were expanded in a planewave basis set with a kinetic energy cutoff of 400 eV. The energy stopping criterion was set to EDIFF = 1E-6 eV. The geometry optimization convergence was set to forces acting on the ions that were smaller than 0.03 eV $Å^{-1}$. Electron-ion interactions were described using the projector augmented wave (PAW) method. [32] Generalized gradient approximation (GGA) of the exchange-correlation energy in the form of Perdew-Burke-Ernzerhof (PBE)[33] was applied together with Grimme D2 dispersion correction.[34] We used the DFT+U approach to describe the localized d-orbitals of Cu ions. The effective Coulomb (U) and exchange (J) terms were set to 4 and 1 eV, respectively.[35] Such a combination of U and J was already successfully applied for very similar systems.[36] Monkhorst-Pack[37] Γ-centered grid with 2×2×4 dimension was used for K-point sampling of the Brillouin zone during the geometry optimization procedure. Different Cu oxidation states were obtained by the introduction of Na cations into the lattice close to the Cu nodes.

Electronic band structures and densities of states were calculated on the VASP optimized systems using Crystal17 software.[38,39] For Raman simulations, atomic positions were reoptimized using PBE0 functional[40] and Grimme D3 dispersion correction.[41]Band structures were calculated using HSE06 functional. [42] Monkhorst-Pack Γ-centered grid with 3×3×18 dimension was used together with POB-TZVP basis set for all atoms.[43]

ASSOCIATED CONTENT

Supporting Information

UV-vis spectra; comparison of calculated and experimental Raman spectra; SEM images; additional Electrochemical-Raman spectra; details of the ICP-MS measurements and TOF calculation; redox titration curve and electrochemical of

CuPc monomer, calculated spectra, bandgaps and DOS of different oxidation states. All simulated systems are provided as cif files.

The Supporting Information is available free of charge on the ACS Publications website.

ECRaman2DMOFs_SI.pdf

AUTHOR INFORMATION

Corresponding Author

*Lehrstuhl für Elektrochemie, Fakultät für Chemie und Lebensmittelchemie, Technische Universität Dresden, Andreas-Schubert-Bau, Zellescher Weg 19, 01069 Dresden, Deutschland
E-mail: inez.weidinger@tu-dresden.de

ACKNOWLEDGMENT

The authors acknowledge financial support from the German Research Foundation (CRC1415 (417590517)), BA 4277/11-1 and EXC 2008/1 (UniSysCat) -390540038).
A.K. and P.P. acknowledge the GWK support for funding this project by providing computing time through the Center for Information Services and HPC (ZIH) at TU Dresden.

REFERENCES

(1) Peera, S. G.; Lee, T. G.; Sahu, A. K. Pt-Rare Earth Metal Alloy/Metal Oxide Catalysts for Oxygen Reduction and Alcohol Oxidation Reactions: An Overview. *Sustainable Energy Fuels* **2019**, *3* (8), 1866–1891.

(2) Shi, Q.; Zhu, C.; Du, D.; Lin, Y. Robust Noble Metal-Based Electrocatalysts for Oxygen Evolution Reaction. *Chem. Soc. Rev.* **2019**, *48* (12), 3181–3192.

(3) Qin, Y.; Ou, Z.; Xu, C.; Zhang, Z.; Yi, J.; Jiang, Y.; Wu, J.; Guo, C.; Si, Y.; Zhao, T. Progress of Carbon-Based Electrocatalysts for Flexible Zinc-Air Batteries in the Past 5 Years: Recent Strategies for Design, Synthesis and Performance Optimization. *Nanoscale Res. Lett.* **2021**, *16* (1).

(4) Wu, J.; Liu, B.; Fan, X.; Ding, J.; Han, X.; Deng, Y.; Hu, W.; Zhong, C. Carbon-Based Cathode Materials for Rechargeable Zinc-Air Batteries: From Current Collectors to Bifunctional Integrated Air Electrodes. *Carbon Energy* **2020**, *2* (3), 370–386.

(5) Pan, J.; Tian, X. L.; Zaman, S.; Dong, Z.; Liu, H.; Park, H. S.; Xia, B. Y. Recent Progress on Transition Metal Oxides as Bifunctional Catalysts for Lithium-Air and Zinc-Air Batteries. *Batter. Supercaps.* **2019**, *2* (4), 336–347.

(6) Wang, J.; Hu, H.; Zhang, H.; Zhao, J.; Li, X.; Song, Z.; Ding, J.; Deng, Y.; Han, X.; Hu, W. Regulating the Catalytically Active Sites in Low-Cost and Earth-Abundant 3d Transition-Metal-Based Electrode Materials for High-Performance Zinc-Air Batteries. *Energy Fuels* **2021**, *35* (8), 6483–6503.

(7) Liu, D.; Tao, L.; Yan, D.; Zou, Y.; Wang, S. Recent Advances on Non-Precious Metal Porous Carbon-Based Electrocatalysts for Oxygen Reduction Reaction. *ChemElectroChem* **2018**, *5* (14), 1775–1785.

(8) Sibul, R.; Kibena-Põldsepp, E.; Ratso, S.; Kook, M.; Sougrati, M. T.; Käärik, M.; Merisalu, M.; Aruväli, J.; Paiste, P.; Treshchalov, A.; Leis, J.; Kisand, V.; Sammelselg, V.; Holdcroft, S.; Jaouen, F.; Tammeveski, K. Iron- and Nitrogen-Doped Graphene-Based Catalysts for Fuel Cell Applications. *ChemElectroChem* **2020**, *7* (7), 1739–1747.

(9) Jasinski, R. A New Fuel Cell Cathode Catalyst. *Nature* **1964**, *201* (1963), 1212–1213.

(10) Li, H.; Sui, Z. An: In Situ Coupling Strategy for the Preparation of Heterometal-Doped Carbon Frameworks as Efficient Bifunctional ORR/OER Electrocatalysts. *New J. Chem.* **2019**, *43* (46), 17963–17973.

(11) Li, C.; Huang, T.; Huang, Z.; Sun, J.; Zong, C.; Yang, J.; Deng, W.; Dai, F. A Sulfonated Cobalt Phthalocyanine/Carbon Nanotube Hybrid as a Bifunctional Oxygen Electrocatalyst. *Dalt. Trans.* **2019**, *48* (46), 17258–17265.

(12) Liu, Y.; Li, Z.; Sun, C.; Wang, S.; Wang, L.; Niu, X.; Sun, P.; Zhang, S. Closely Packed Planar Polyphthalocyanine Iron/Hierarchical Three-Dimensional Graphene as an Oxygen Electrocatalyst for the ORR and OER, and Zinc-Air Batteries. *Sustain. Energy Fuel* **2021**, *5* (20), 5216–5226.

(13) Cheng, W.; Yuan, P.; Lv, Z.; Guo, Y.; Qiao, Y.; Xue, X.; Liu, X.; Bai, W.; Wang, K.; Xu, Q.; Zhang, J. Boosting Defective Carbon by Anchoring Well-Defined Atomically Dispersed Metal-N4 Sites for ORR, OER, and Zn-Air Batteries. *Appl. Catal. B* **2020**, *260*, 118198.

(14) Serov, A.; Andersen, N. I.; Roy, A. J.; Matanovic, I.; Artyushkova, K.; Atanassov, P. CuCo 2 O 4 ORR/OER Bi-Functional Catalyst: Influence of Synthetic Approach on Performance . *J Electrochem. Soc.* **2015**, *162* (4), F449–F454.

(15) Zhang, T.; Wang, C.; Liu, S.; Wang, J. L.; Lin, W. A Biomimetic Copper Water Oxidation Catalyst with Low Overpotential. *J. Am. Chem. Soc.* **2014**, *136* (1), 273–281.

(16) Huang, H.; Lan, Z.; Li, W.; Mo, W.; Zhao, L.; Zhang, J. A Novel and Low-Cost CuPc@C Catalyst Derived from the Compounds of Sunflower Straw and Copper Phthalocyanine Pigment for Oxygen Reduction Reaction. *RSC Adv.* **2021**, *11* (26), 15590–15597.

(17) Furukawa, H.; Cordova, K. E.; O'Keeffe, M.; Yaghi, O. M. The Chemistry and Applications of Metal-Organic Frameworks. *Science (1979)* **2013**, *341* (6149).

(18) Wang, M.; Dong, R.; Feng, X. Two-Dimensional Conjugated Metal-Organic Frameworks (2Dc-MOFs): Chemistry and Function for MOFtronics. *Chem. Soc. Rev.* **2021**, *50* (4), 2764–2793.

(19) Zhao, K.; Zhu, W.; Liu, S.; Wei, X.; Ye, G.; Su, Y.; He, Z. Two-Dimensional Metal-Organic Frameworks and Their Derivatives for Electrochemical Energy Storage and Electrocatalysis. *Nanoscale Adv.* **2020**, *2* (2), 536–562.

(20) Yu, M.; Dong, R.; Feng, X. Two-Dimensional Carbon-Rich Conjugated Frameworks for Electrochemical Energy Applications. *J. Am. Chem. Soc.* **2020**, *142* (30), 12903–12915.

(21) Zhong, H.; Wang, M.; Chen, G.; Dong, R.; Feng, X. Two-Dimensional Conjugated Metal-Organic Frameworks for Electrocatalysis: Opportunities and Challenges. *ACS Nano.* **2022**, *16* (2), 1759–1780.

(22) Kielb, P.; Horch, M.; Wrzolek, P.; Goetz, R.; Ly, K. H.; Kozuch, J.; Schwalbe, M.; Weidinger, I. M. Hydrogen Evolution by Cobalt Hangman Porphyrins under Operating Conditions Studied by Vibrational Spectro-Electrochemistry. *Catal. Sci. Techno.* **2018**, *8* (7), 1849–1857.

(23) Ly, H. K.; Wrzolek, P.; Heidary, N.; Götz, R.; Horch, M.; Kozuch, J.; Schwalbe, M.; Weidinger, I. M. 2nd Coordination Sphere Controlled Electron Transfer of Iron Hangman Complexes on Electrodes Probed by Surface Enhanced Vibrational Spectroscopy. *Chem. Sci.* **2015**, *6* (12), 6999–7007.

(24) Ly, K. H.; Weidinger, I. M. Understanding Active Sites in Molecular (Photo)Electrocatalysis through Complementary Vibrational Spectroelectrochemistry. *Chem. Comm.* **2021**, *57* (19), 2328–2342.

(25) Wang, Z.; Walter, L. S.; Wang, M.; Petkov, P. S.; Liang, B.; Qi, H.; Nguyen, N. N.; Hambsch, M.; Zhong, H.; Wang, M.; Park, S.; Renn, L.; Watanabe, K.; Taniguchi, T.; Mannsfeld, S. C. B.; Heine, T.; Kaiser, U.; Zhou, S.; Weitz, R. T.; Feng, X.; Dong, R. Interfacial Synthesis of Layer-Oriented 2D Conjugated Metal-Organic Framework Films toward

Directional Charge Transport. *J. Am. Chem. Soc.* **2021**, *143* (34), 13624–13632.

(26) Wang, Z.; Liu, D.; Gu, H.; Zhu, A.; Tian, Y.; Shi, G. NTA-Modified Carbon Electrode as a General Relaying Substrate to Facilitate Electron Transfer of SOD: Application to in Vivo Monitoring of O2- in a Rat Brain. *Biosens. Bioelectron.* **2013**, *43* (1), 101–107.

(27) Zhong, H.; Ly, K. H.; Wang, M.; Krupskaya, Y.; Han, X.; Zhang, J.; Zhang, J.; Kataev, V.; Büchner, B.; Weidinger, I. M.; Kaskel, S.; Liu, P.; Chen, M.; Dong, R.; Feng, X. A Phthalocyanine-Based Layered Two-Dimensional Conjugated Metal–Organic Framework as a Highly Efficient Electrocatalyst for the Oxygen Reduction Reaction. *Angew. Chem. Int. Ed.* **2019**, *58* (31), 10677–10682.

(28) Sun, T.; Li, Y.; Cui, T.; Xu, L.; Wang, Y. G.; Chen, W.; Zhang, P.; Zheng, T.; Fu, X.; Zhang, S.; Zhang, Z.; Wang, D.; Li, Y. Engineering of Coordination Environment and Multiscale Structure in Single-Site Copper Catalyst for Superior Electrocatalytic Oxygen Reduction. *Nano Lett.* **2020**, *20* (8), 6206–6214.

(29) Deng, Y.; Handoko, A. D.; Du, Y.; Xi, S.; Yeo, B. S. In Situ Raman Spectroscopy of Copper and Copper Oxide Surfaces during Electrochemical Oxygen Evolution Reaction: Identification of CuIII Oxides as Catalytically Active Species. *ACS Catal.* **2016**, *6* (4), 2473–2481.

(30) Zhou, Z.; Li, X.; Li, Q.; Zhao, Y.; Pang, H. Copper-Based Materials as Highly Active Electrocatalysts for the Oxygen Evolution Reaction. *Mater. Today Chem.* **2019**, *11*, 169–196.

(31) Kresse, G.; Furthmüller, J. Efficiency of Ab-Initio Total Energy Calculations for Metals and Semiconductors Using a Plane-Wave Basis Set. *Comput. Mater. Sci.* **1996**, *6* (1), 15–50.

(32) Kresse, G.; Joubert, D. From Ultrasoft Pseudopotentials to the Projector Augmented-Wave Method. *Phys. Rev. B* **1999**, *59* (3), 1758–1775.

(33) Perdew, J. P.; Burke, K.; Ernzerhof, M. Generalized Gradient Approximation Made Simple. *Phys. Rev. Lett.* **1996**, *77* (18), 3865–3868.

(34) Grimme, S. Semiempirical GGA-Type Density Functional Constructed with a Long-Range Dispersion Correction. *J. Comput. Chem.* **2006**, *27*, 1787–1799.

(35) Anisimov, V. I.; Aryasetiawan, F.; Lichtenstein, A. I. First-Principles Calculations of the Electronic Structure and Spectra of Strongly Correlated Systems: The LDA+Umethod. *J. Phys.: Condens. Matter.* **1997**, *9*, 767.

(36) Li, W.; Sun, L.; Qi, J.; Jarillo-Herrero, P.; Dincă, M.; Li, J. High Temperature Ferromagnetism in π-Conjugated Two-Dimensional Metal-Organic Frameworks. *Chem. Sci.* **2017**, *8* (4), 2859–2867.

(37) Monkhorst, H. J.; Pack, J. D. Special Points for Brillouin-Zone Integrations. *Phys. Rev. B* **1976**, *13* (12), 5188–5192.

(38) Dovesi, R.; Erba, A.; Orlando, R.; Zicovich-Wilson, C. M.; Civalleri, B.; Maschio, L.; Rérat, M.; Casassa, S.; Baima, J.; Salustro, S.; Kirtman, B. Quantum-Mechanical Condensed Matter Simulations with CRYSTAL. *Wiley Interdiscip. Rev. Comput. Mol. Sci.* **2018**, *8* (4), e1360.

(39) Dovesi, R.; Saunders, V.; Roetti, C.; Orlando, R.; Zicovich-Wilson, C. M.; Pascale, F.; Civalleri, B.; Doll, K.; Harrison, N.; Bush, I.; Llunel, M.; Causà, M.; Noël, Y.; Maschio, L.; Erba, A.; Rérat, M.; Casassa, S. *CRYSTAL17 User's Manual*; 2018.

(40) Adamo, C.; Barone, V. Toward Reliable Density Functional Methods without Adjustable Parameters: The PBE0 Model. *J. Chem. Phys.* **1999**, *110* (13), 6158–6170.

(41) Grimme, S.; Antony, J.; Ehrlich, S.; Krieg, H. A Consistent and Accurate Ab Initio Parametrization of Density Functional Dispersion Correction (DFT-D) for the 94 Elements H-Pu. *J. Chem. Phys.* **2010**, *132* (15).

(42) Heyd, J.; Scuseria, G. E.; Ernzerhof, M. Hybrid Functionals Based on a Screened Coulomb Potential. *J. Chem. Phy.* **2003**, *118* (18), 8207–8215.

(43) Peintinger, M. F.; Oliveira, D. V.; Bredow, T. Consistent Gaussian Basis Sets of Triple-Zeta Valence with Polarization Quality for Solid-State Calculations. *J. Comput. Chem.* **2013**, *34* (6), 451–459.

Insert Table of Contents artwork here